Composites Science and Technology 207 (2021) 108706

Contents lists available at ScienceDirect

Composites Science and Technology

journal homepage: http://www.elsevier.com/locate/compscitech

Kinematic and mechanical response of dry woven fabrics in through-thickness compression: Virtual fiber modeling with mesh overlay technique and experimental validation

Lode Daelemans [a,*], Brecht Tomme [a], Baris Caglar [b,c], Véronique Michaud [b], Jeroen Van Stappen [d,e], Veerle Cnudde [d,e,f], Matthieu Boone [d,g], Wim Van Paepegem [a]

[a] Department of Materials, Textiles and Chemical Engineering (MATCH), Ghent University, Technologiepark 70A, B-9052, Zwijnaarde, Belgium
[b] Laboratory for Processing of Advanced Composites (LPAC), Institute of Materials (IMX), Ecole Polytechnique Fédérale de Lausanne (EPFL), Station 12, Lausanne, CH, 1015, Switzerland
[c] Aerospace Manufacturing Technologies, Faculty of Aerospace Engineering, Delft University of Technology, Kluyverweg 1, Delft, 2629HS, the Netherlands
[d] Centre for X-ray Tomography (UGCT), Ghent University, Proeftuinstraat 86, B-9000, Ghent, Belgium
[e] Department of Geology, Pore-Scale Processes in Geomaterials Research (PProGRess), Ghent University, Krijgslaan 281/S8, B-9000, Ghent, Belgium
[f] Environmental Hydrogeology, Department of Earth Sciences, Utrecht University, Princetonlaan 8a, 3584, CB, Utrecht, the Netherlands
[g] Department of Physics and Astronomy,Radiation Physics - UGCT, Ghent University, Proeftuinstraat 86, B-9000, Ghent, Belgium

ARTICLE INFO

Keywords:
A. Fabrics/textiles
B. Mechanical properties
C. Finite element analysis (FEA)
D. X-ray computed tomography
Digital element analysis

ABSTRACT

The through-thickness compressive behavior of fabric reinforcements is crucial in liquid composite molding manufacturing processes. Predictive simulations of the compressive response are thus necessary to enable a virtual processing workflow. These are complex however, as the compressive behavior of the reinforcement fabrics is non-linear. Altough virtual fiber modeling has proven to be a strong kinematical tool, it cannot predict the compressive response due to the lack of bending stiffness in the virtual fibers. Here, we describe a solution that enables predictive compressive simulations through hybrid virtual fibers. It is based on an overlay mesh-element technique, combining both (i) finite elements that determine the in-plane fiber properties as well as (ii) finite elements that determine out-of-plane fiber bending. Using these hybrid virtual fibers, the through-thickness compression of a twill woven fabric ply is simulated and experimentally validated using both μCT-based as compliance-based measurements. Excellent agreement between simulation and experiment is obtained for the right set of input parameters.

1. Introduction

Liquid Composite Molding (LCM) processes such as Vacuum Assisted Resin Transfer Molding (VARTM), Resin Transfer Molding (RTM), or Injection Compression Molding (ICM), are composite manufacturing processes in which a dry fibrous reinforcement is infused with liquid resin. The permeability of the fibrous reinforcement is key to allow sufficient flow of resin throughout the reinforcement, resulting in high-quality parts that are used in industry, for example in the automotive, marine, and civil sectors. The flow is usually dual-scaled, with micro-porous channels between reinforcing fibers, and meso-porous channels dependent on the reinforcement textile structure each affecting the flow [1]. Moreover, the reinforcement is compressed between two mold halves in LCM processes and its microstructure hence changes because of the applied pressure (e.g. tow compaction). Hence, understanding and predicting the through-thickness compression behavior of reinforcements is one of the crucial factors in the manufacturing of high-quality composite parts through LCM processes.

A large body of research is devoted to experimental analysis of the through-thickness compression of fabrics and typically relies on extensive high-resolution X-ray micro-computed tomography (μCT) analysis to determine the structure of reinforcement textiles under pressure [1–8]. Although modeling techniques would provide a good alternative, the fibrous nature of textile reinforcements complicates out-of-plane properties such as through-thickness compression due to dominant deformation mechanisms on the microscale such as fiber realignment. Although macro- and mesoscale models exist, these are usually fitted with specific constitutive laws based on experimentally determined

* Corresponding author.
E-mail address: lode.daelemans@ugent.be (L. Daelemans).

https://doi.org/10.1016/j.compscitech.2021.108706
Received 31 July 2020; Received in revised form 30 January 2021; Accepted 3 February 2021
Available online 7 February 2021

through-thickness input properties [9]. In addition, they do not reveal conclusions about the micro-level which would be relevant for microscale permeability.

Microscale models offer the possibility to analyze the through-thickness compression at the reinforcement level while taking into account the microscale deformation mechanisms. Most notably, the virtual fiber modeling method, initially conceived by Wang et al. [10,11], is proving to be one of the most viable options. Often referred to as the digital element method, this method is centered around the modeling of fibers through a chain of truss-like elements (digital elements), simulating the textile material as made up of a relatively small amount of such "virtual" fibers (up to 100–200). The virtual fiber method thus explicitly takes into account the fibrous behavior of the reinforcements at near-microscale.

Recently, multiple researchers have shown that the virtual fiber modeling of textile reinforcements captures relevant deformation mechanisms such as the yarn cross-sectional deformation and yarn path waviness and that the predicted microstructures correlate well to those observed by μCT imaging [12–17]. Yet, the kinematic nature of the simulations limits their ability to link the mechanics with the kinematics, e.g. to simulate pressure-dependent microstructure. This is especially true in the case of out-of-plane loadings such as compression, where the reinforcement response is dominated by fiber bending and by creation of new contact surfaces due to fiber realignment. In the case of in-plane loadings, the response is dominated by tensile loading in the fiber directions and we have previously reported a successful correlation between kinematics and mechanics for these cases [18,19]. The virtual fiber modeling method has recently been applied to through-thickness compression of woven fabrics with successful validation of the microstructure (e.g. yarn compaction, yarn paths, …) to experimental data [20,21]. Yet in both cases, the modeling is kinematic only in that the compaction in the models is realized without taking the actual pressure level into account. Although this enables meso-scale models to include the correct mechanical behavior by using the predicted microstructures [21], virtual fiber modeling with correct out-of-plane mechanics might provide a more efficient route for virtual mechanical analysis of textile reinforcements.

The benefits of the virtual fiber modeling approach over the wider used meso-scale approach, e.g. Refs. [9,22,23], can be summarized as:

(i) The initial yarn shape and configuration in the textile fabric can be simulated, and thus does not require any a priori shape assumptions (e.g. elliptical, lenticular, …cross-sections) nor dedicated geometry extraction from microscopic images (e.g. micro-computed tomography).
(ii) The transversal behavior related to the realignment of fibers within the yarn under load is naturally implemented without requiring dedicated material constitutive laws. In essence, this enables to directly take into account yarn specific properties, for example, yarn twist or the use of multiple fiber types within a yarn, instead of recalibrating the constitutive laws. Moreover, there is also an option to use a virtual fiber modeling approach to determine the input properties for mesoscopic and macroscopic models, e.g. such as developed in Refs. [22,24,25], creating a stronger virtual textile modeling workflow.
(iii) The discrete nature of the yarn consisting out of many fibers offers more deformation modes. In comparison, meso-scale models could run into problems under severe yarn deformations where the continuum approach does not suffice, e.g. where yarns would flatten out, unravel or split. Such loadings can be encountered for example in process modeling where the yarns come into contact with surfaces or tools (e.g. tufting needles, mold surfaces, sharp corners, …).

These advantages make that the virtual fiber modeling approach has its benefits to co-exist alongside meso-scale modeling, where it allows an additional level of detail situated between the micro- and the meso-scale.

In this paper, we describe a framework to enable the correct inclusion of fiber bending into the virtual fiber modeling approach, to predict the through-thickness compression of a twill woven glass fibre fabric reinforcement. It is based on an overlay mesh-element technique, combining both (i) finite elements that determine the in-plane fiber properties as well as (ii) finite elements that determine out-of-plane fiber bending. This method is applied to the through-thickness compression of a single layer of dry fabric reinforcement to exclude any effects by the nesting of multiple layers. To validate the model, two different test methods are used to determine the pressure-compaction relationship for a single reinforcement ply with adequate resolution.

2. Simulation details

2.1. Generation of an as-woven state

Starting from an idealized unit cell geometry, the as-woven state of the twill fabric is generated using the virtual fiber principle as reported for example in our earlier work for 3D woven fabrics within the Abaqus 2019 Finite Element Analysis environment [18] (Fig. 1). Briefly, an idealized and "loose" unit cell geometry, based on the values reported in Table 1, is created. A shrinkage step then creates tensile forces in the yarns similar to those present in an actual weaving step. By tensioning the yarns, the fibers will realign and spread out, creating the typical lenticular yarn cross-sectional shapes. This results in the as-woven state of the fabric. Periodicity of the unit cell is ensured using periodic boundary conditions proposed by Green et al. [15] and Thompson et al. [21], consisting of periodicity imposed at individual fiber ends as well as slave yarns that provide a contact surface at the unit cell edges.

Here, the virtual fibers consist of chains of linear elastic truss elements (T3D2 elements, Abaqus/Explicit) with properties representing glass fiber properties. All input properties that are used are related to actual physical and measurable parameters (see Table 1). Note that the majority of these parameters can already be found in the datasheets of the fiber and fabric material, making extended experimental characterization unnecessary.

The diameter of the virtual fibers D_{vf} (circular cross-section) is chosen such that the physical cross-sectional area of the virtual and real yarn, A_{vy} and A_{ry} are equal:

$$A_{vy} = n_{vf}\frac{\pi}{4}D_{vf}^2 = A_{ry} = n_{rf}\frac{\pi}{4}D_{rf}^2 \rightarrow D_{vf} \quad (1)$$

where n_{vf} and n_{rf} are the number of fibers in the virtual and in the real yarn, and, D_{rf} is the diameter of the fibers in the real yarn (which can be measured, or calculated from the tex-value of the fibers if the density is known).

Since the cross-sectional area is equal, volumetric properties such as the Young's modulus or tensile strength of the real fibers can be assigned to the virtual fibers as well. Surface properties, such as frictional constants, however, will be affected by the discretization of the yarns into a relatively low amount of virtual fibers (30–130, compared to the thousands of fibers in an actual yarn). The yarn-to-yarn friction for glass fiber yarns is reported to vary between 0.2 and 0.4 depending on the tension and normal pressure applied to the yarns, their velocity (static versus dynamic friction), and the sliding directions (parallel or transverse to each other) [26]. Generally, lower friction coefficients are found at higher velocities and forces, such as may be encountered during weaving. Therefore, it was decided to impose a friction coefficient of 0.2 in our as-woven simulations. Contacts are handled by the *General Contact* algorithm in Abaqus between the fiber surfaces. The final as-woven state is reached by imposing a shrinkage factor on the yarns in the "loose-state" such that the final crimp of the yarns is equal to the experimentally determined crimp.

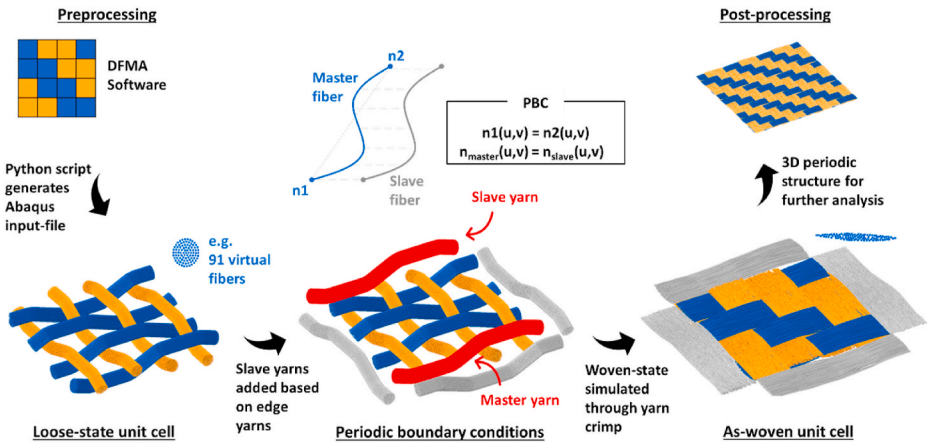

Fig. 1. Conceptual overview of the as-woven fabric generation using the virtual fiber principle and periodic boundary conditions.

Table 1
Input properties used in the simulations obtained from measurements, calculations, or datasheet values. Values between brackets are datasheet values.

Property	Warp	Weft	Property determination
FIBERS			
Linear density (dTex)	1.57		Measured according to ISO 1973 (vibroscope)
Average fiber diameter (μm)	8.9 (9)		Calculated from linear density and volumetric density.
Volumetric density (kg m^{-3})	(2550)		Datasheet value.
E-modulus (cN/dTex | GPa)	292 | 74.6		Measured according to ASTM D3822.
YARNS			
Linear density (Tex)	338 (340)	269 (272)	Measured according to ISO 7211-5.
Fibers per yarn (–)	2148	1708	Calculated from linear densities of yarn and fiber.
Bending stiffness (10^{-7} Nm^2)	1.49	0.99	Measured according to ASTM D1388.
FABRIC			
Areal density (g m^{-2})	387 (390)		Measured.
Thread count (cm^{-1})	6.1 (6.0)	6.5 (6.7)	Measured according to ISO 7211-2.
Yarn spacing (cm)	0.164	0.154	Calculated from thread count.
Crimp (%)	0.55	0.75	Measured according to ISO 7211-3.

The idealized unit cell geometry is created through the Dynamic Fabric Mechanical Analyzer (DFMA, www.fabricmechanics.com) from the Fabric Mechanics group at Kansas State University (Wang et al.), who originally published the virtual fiber principle in Refs. [10,11]. Although the software itself is capable of mechanical analysis, the simulations in this work are performed using the finite element analysis package Abaqus as it allows the use of an explicit solver, a mesh overlay technique (see Section 2.2) and more complex boundary and contact conditions. The DFMA software was thus used here only as a pre-processor; the idealized geometry is generated in DFMA and then exported through a dedicated python script to an Abaqus 2019 input file for the as-woven simulation.

The initial loose-state unit cell consists of fibers and yarns in a curved position. As such, truss element based virtual fibers (which have no bending stiffness) are perfectly suited. In fact, implementation of bending stiffness at this step would only result in spurious stresses as the virtual fibers would want to relax back to their initial, and thus curved, positions. In reality, yarns entering a weaving loom are straight instead of curved and are subsequently deformed to form the as-woven state.

2.2. Overlay mesh technique and compression simulation

Bending stiffness is imposed on the virtual fibers by overlaying the truss elements with beam elements (B31, Abaqus/Explicit) using the same nodes, see Fig. 2a. This creates hybrid virtual fibers in which the truss elements will determine the properties in the fiber direction (tensile stiffness), while the beam elements are chosen such that they do not affect those properties (negligible Young's modulus), but have a certain bending stiffness EI. The value of that bending stiffness can be set to the required value by changing either the Young's modulus E or the beam element radius which defines its second moment of inertia I ($= \pi r^4$). Here we opted to fix the Young's modulus such that $E_{truss} = 100\, E_{beam}$ to suppress any effects that might rise from the stiffness of the beam elements. For the range of EI considered, the beam radius was similar to that of the truss elements, ensuring that the overall tensile stiffness of the virtual fibers was barely affected by the superimposed beam elements. The virtual fiber bending stiffness was set as follows:

$$n_{vf} E_{beam} I_{vf,beam} = (EI)_{measured} \tag{2}$$

The through-thickness compression is simulated by two rigid platens (rigid shell elements R3D4, Abaqus/Explicit) which move towards each other (displacement-controlled) with the fabric reinforcement in between, see Fig. 2b. The simulation is performed under quasi-static conditions in Abaqus 2019 Explicit (the internal energy is much higher than the kinetic energy). Contact between the virtual fiber surfaces and their surroundings (other fibers and compression platens) is imposed on the truss elements only and is defined by Abaqus' *General Contact* algorithm. The beam elements are excluded from any contact definition as their radius is dependent on the required bending stiffness and does not represent the fiber radius, the fiber radius is equal to the truss element radius. During compression of the as-woven fabric, the reaction forces on the platens and the distance between them are used to determine the pressure-thickness and pressure-volume fraction curves. The same periodic boundary conditions as before are used.

3. Experimental details

3.1. Fiber, yarn and fabric properties

Table 1 gives an overview of all the properties of the dry glass fiber twill fabric (Interglas 92140 aero, finish FK 144, 2 × 2 twill woven, 390 g/m^2, purchased through R&G Faserverbundwerkstoffe GmbH, Waldenbuch, Germany) that serve as input for the simulations. Several properties are measured experimentallyt, instead of relying on averaged datasheet values, to achieve higher accuracy of the simulations. Note that the majority of the required input properties are usually given in the datasheet of the fabric and fiber material, or are relatively easy to

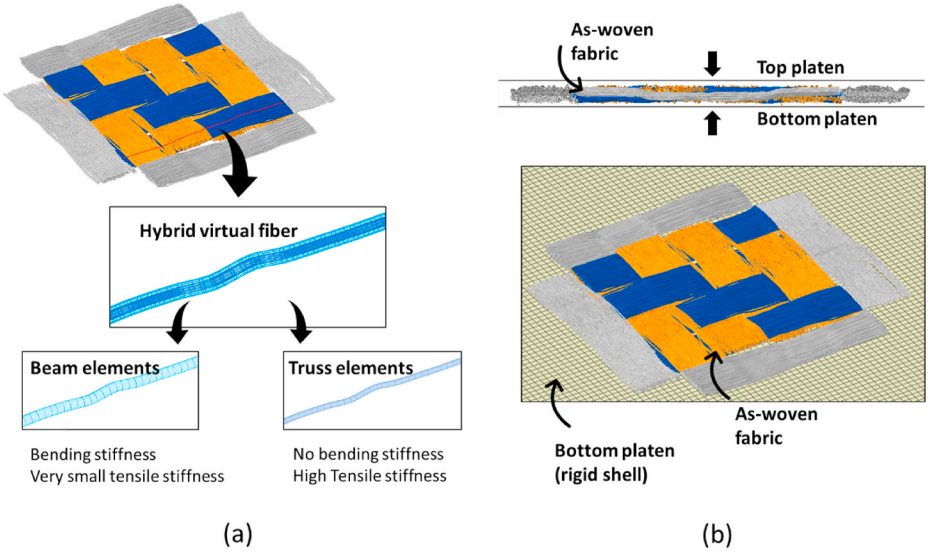

Fig. 2. (a) The fabric is constructed of hybrid virtual fibers that consist of a chain of beam elements for bending stiffness and truss element for tensile stiffness. (b) Overview of the through-thickness compression setup (for clarity the top platen is hidden in the overview image).

determine/calculate. Only the bending stiffness of the yarns is usually not given and has to be measured for example by Peirce's cantilever method. This method is relatively simple and barely requires any investment in machinery.

3.2. Through-thickness compression testing

We opted for two different ways to measure the through-thickness compressive response of a single fabric layer due to the difficulty in achieving the required platen-to-platen distance accurately enough: (i) using a compliance-calibration and self-aligning compression setup (setup 1, Fig. 3a, available at Ecole Polytechnique Fédérale de Lausanne), and, (ii) using in-situ X-ray micro-computed tomography (μCT) with a dedicated compression cell that allows imaging of specimens during mechanical loading (setup 2, Fig. 3b, available at Ghent University).

Setup 1 consists of two steel platens, the lower one a square surface of 100 mm × 100 mm and connected to a universal testing machine (Walter + Bai LFM-125kN equipped with a 10 kN load cell) with a fixed support [27]. The upper platen has a circular surface with a diameter of 45 mm and contains a ball-pivot system for self-alignment that maintains parallelism between the lower and upper platens. A single layer of fabric cut to dimensions of 60 mm × 60 mm was compressed between the platens. Each compression measurement on this setup is preceded by a measurement without a specimen. The calibration curve obtained in the measurement without a specimen is used for compliance correction of the following compression measurement. Compliance correction is performed, for all recorded force values in the compression test, by subtracting the corresponding thickness in the compliance test from the thickness in the compression test [28].

Setup 2 consists of two machined poly-ether-ether-ketone (PEEK) compression platens that are attached to an in-situ mechanical stage (CT5000, Deben, Suffol, United Kingdom) in combination with an internal load cell of 1 kN. A step-and-shoot procedure is followed to obtain μCT datasets of the fabric layer and the spacing between the compression platens. At different pressure levels, each μCT scan is made in approximately 10 min using the Environmental Micro-CT system (EMCT) at Ghent University [29]. During this time, the position of the compression platens remains stationary, and a slight relaxation of the pressure by 1.5% of the set pressure value was observed for the two

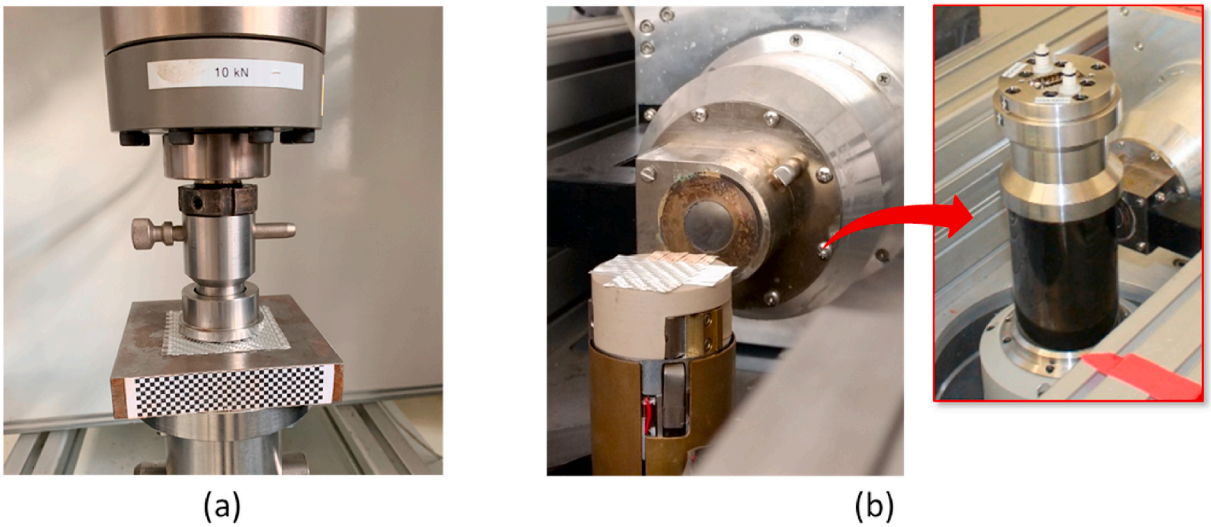

Fig. 3. (a) Setup 1: self-aligning compression setup, (b) Setup 2: in-situ compression setup for μCT measurements.

highest pressure levels. No movement artefacts were observed in the μCT scan, indicating that the relaxation in the sample and PEEK compression platens during scanning were smaller than the image resolution, and thus did not affect imaging. For each scan, a total of 1440 projection images are acquired during a rotation of the scanner setup around the object from 0° to 360°. The X-ray source is operated with a source accelerating voltage of 80 kV, with a power of 8 W. Tomographic reconstruction is performed using Octopus Reconstruction [30]. The load is recorded by the CT5000 testing stage and combined with the displacement data measured on the μCT images.

The fabric under consideration has a thickness of approximately 0.5 mm in a non-compressed state and is compressed to approximately 0.25 mm. Hence, to have an adequate pressure-thickness or pressure-volume fraction curve, the distance between the compression platens needs to be accurately monitored at the micrometer scale. Studies often analyze the compressive properties by compression of multiple layers of reinforcement, e.g. Refs. [31–33]. This is advantageous for the platen-to-platen measurement accuracy since it results in a larger spacing between the compression platens, which in turn allows for the use of less sensitive displacement measurements such as the crosshead displacement. Nevertheless, the resulting compression curve is not representative for a single ply of reinforcement due to nesting of the layers and thus cannot be used to validate the model here.

In addition to the compressive experiments, four composite specimens were produced by compression molding of a single fabric reinforcement layer between two flat plates under a pressure of 0.0, 0.5, 0.12 and 0.25 MPa applied by stacking weights on top of the plate. These specimens were then cured at room temperature (matrix resin is EPIKOTE MSG RIMR 135 and EPIKURE MGS RIMH 137 from Momentive Performance Materials, Hemiksem, Belgium) and subsequently μCT images were obtained to determine the thickness of the specimens.

4. Results and discussion

4.1. Generation of the as-woven state through virtual fiber modeling

Fig. 4 represents the as-woven states for yarns made up of 61 and 91 virtual fibers. These numbers were based on earlier work. For example, Green et al. [15] studied the effect of the number of virtual fibers per yarn, going from 19 to 91, and indicated that at least two or three virtual fibers across the thickness of the yarns in their deformed state where required for sufficient accuracy. In their case, a 61 fiber model represented the best compromise between analysis time and accuracy, and only very minor improvements were noted using 91 fibers. Similarly, the results in Fig. 4 indicate that 61 virtual fibers suffice here as well.

The predicted fabric geometry (fabric thickness, yarn widths, cross-sectional shapes) corresponds well to that of the actual fabric. The as-woven state is simulated using the Abaqus/Explicit solver with dynamics similar to the actual weaving process: a step time of 0.06 s corresponding to a weaving speed of 1000 picks/min, a typical value for projectile, rapier and air-jet looms. Three different length-to-diameter ratios for the truss elements and beam overlay elements were investigated, i.e. L/D equals 0.5, 1, or 3 (see Section 4.3.1). The *General Contact* algorithm in Abaqus 2019 performed well for each L/D ratio considered here and contact/collision detection remained robust even for much larger L/D ratios. Nevertheless, large L/D ratios are not feasible as they would affect the "flexibility" of a virtual fiber (in the digital element method, material properties are induced by discretization into elements, in contrast to finite element modeling where they are defined by the material constitutive laws).

4.2. Experimental determination of the through-thickness compressive response of a single fabric layer

The compressive response of the fabric measured according to the different methods/setups explained in Section 3.2 is given in Fig. 5 (fiber volume fraction was determined based on the fiber density, fabric areal density and platen-to-platen distance). Overall, the curves show an exponentially increasing pressure for higher compression levels as expected. As a comparison, the thickness of the molded composite specimens are added as well (red datapoints).

The compliance calibration procedure using crosshead displacement data seems to result in an underestimation of the platen-to-platen distance (fabric thickness), especially in the low compression regime (here 0.0–0.2 MPa). This could have several causes, e.g. (i) the platen-to-platen misalignment is not identical during recording of the calibration curve and the specimen curves, or, (ii) the set-up compliance is not perfectly reproducible due to spurious misalignments in the fixtures or testing machine. Since there is no physical measurement of the actual platen-to-platen distance, it remains difficult to asses whether the response in the low compression regime can be considered correct.

Using in-situ μCT during compressive testing did allow to determine the physical platen-to-platen distance at each pressure level from the

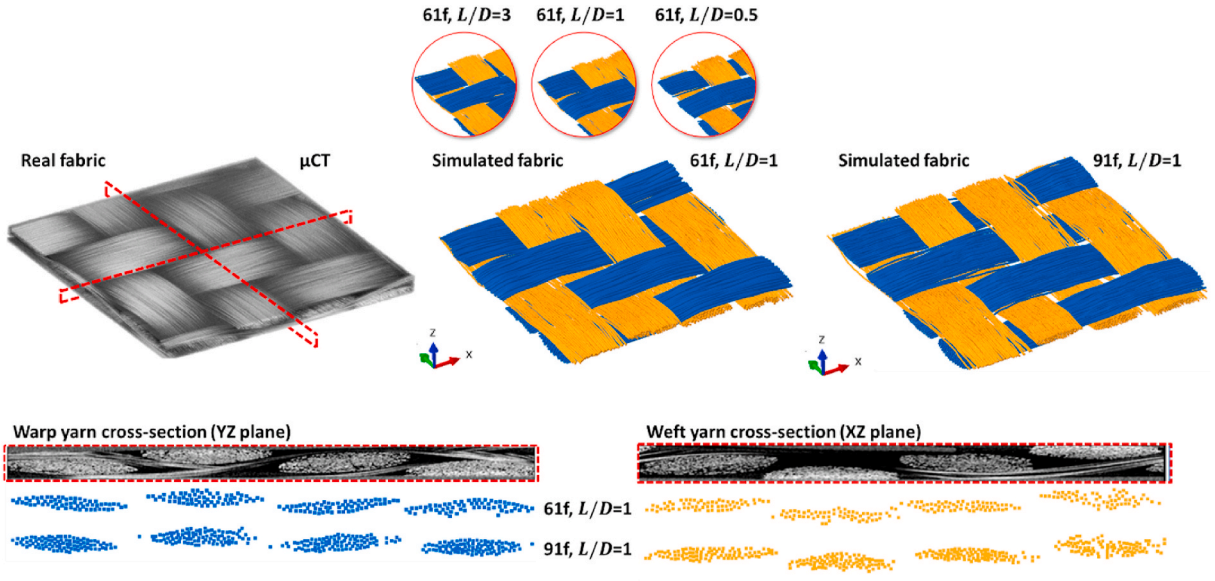

Fig. 4. Comparison of real fabric from μCT experiments (left) and simulated fabric (micro-)geometry (right) shows good visual agreement between both.

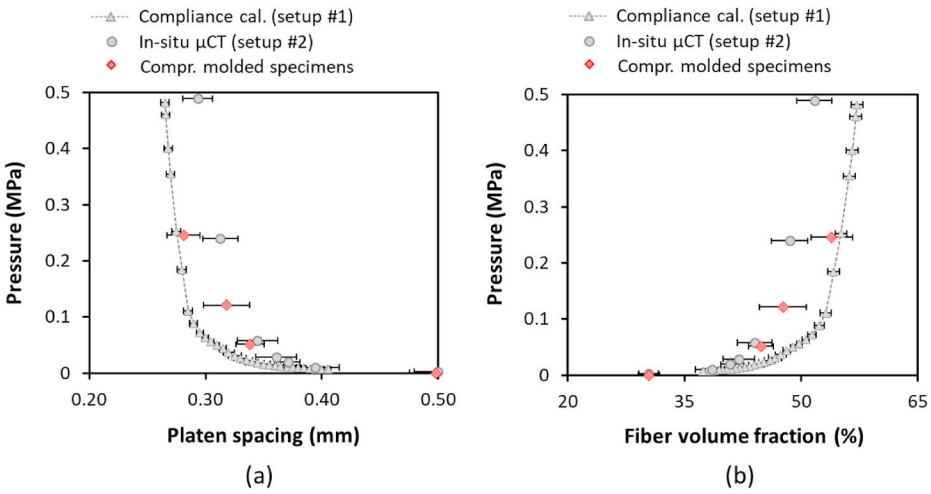

Fig. 5. (a) Pressure versus platen spacing and (b) pressure versus fiber volume fraction obtained by the three different setups. These results clearly illustrate the difficulty associated with measuring the through-thickness compressive response of a single fabric layer with adequate certainty.

µCT images (Fig. 6). There is good agreement with the results from the compression molded specimens, especially in the low pressure regime. At the specimen size required for sufficient unit cells to be loaded under compression, however, the resolution of the µCT-scans is approximately 15 µm. Moreover, the use of the in-situ compression test set-up and the limited platen-to-platen distance (platens made from PEEK polymer) inevitably lowered the quality of the µCT images. This means that there is an uncertainty of 1–2 voxels on the determination of the borders of the compression platens, which results in the relatively large error bars compared to the compliance calibration method in Fig. 5. In comparison to the compliance calibration method, the compression set-up used in the µCT scanner is not self-aligning and maintains a fixed platen misalignment of approximately 0.25° in both warp and weft direction (determined on the µCT images).

Overall, the experimental compressive response of one reinforcement ply remains difficult to assess with adequate certainty. Therefor, the range described by both the compliance calibration and the in-situ µCT method is considered as the validation window for the simulations.

4.3. Simulating the through-thickness compressive response

4.3.1. Mesh convergence

Although the simulation of the as-woven state is not affected much by the considered L/D-ratios, this is different for the compression simulations using the beam element overlay (Fig. 7a). During compression, virtual fibres are bent around other off-axis virtual fibers. Hence, the element length needs to be similar to the virtual fiber diameter to conform to the geometry of the neighboring off-axis fibers. The (bending) strain energy of the superimposed beam elements was indeed higher for L/D ratios of 1 and 0.5 compared to a ratio of 3, indicating a higher degree of bending happening in the virtual fibres for L/D ratios of 1 and 0.5. This explains why a stiffer compaction response is recorded for these simulations. Here an L/D ratio ≤ 1 sufficed to achieve convergence of the simulations using 61 virtual fibres, and $L/D = 1$ is selected for further simulations (reduced computational resources compared to $L/D = 0.5$).

Beside the element length, the number of virtual fibers can also be seen as a mesh convergence parameter (e.g. dividing the yarn into a very small amount of virtual fibers would not lead to the same results). The results (Fig. 7b) show that the difference for 61 and 91 fibers is small, taking into account that both simulations are run with the same frictional constant albeit that the yarns have a differing internal frictional surface (more detailed explanation in **Section 4.3.3**). Hence, we can assume that the compression simulations have also converged at 61 virtual fibers. This is in close agreement with the required number of virtual fibers reported by other research groups [34,35]. Note that a compression simulation for 61 virtual fibers with $L/D = 1$ took about 6 h of calculation time on a regular PC (Intel® Core™ i7-3770 3.40 GHz, 4 cores, 16.0 GB RAM, SSD hard disk). For the 91 virtual fibres, a difference in compression response is obtained above 0.2 MPa for $L/D = 0.5$ and $L/D = 1$. Closer inspection of the results showed that for $L/D = 1$ a higher amount of contact penetrations occurred at high compaction level than for $L/D = 0.5$, resulting in an (artificially) lower stiffness. This is explained in more detail in Section 4.3.5.

The correspondence between the predicted and the experimentally determined compaction response is good, especially at low compaction levels (up to 0.28 mm platen spacing). This indicates that the compaction process is well captured by the virtual fibers, even though there are size and number differences between the virtual and real fibers which could lead to a difference in compaction (smaller fibers can compact more densely than large fibers). In addition, simulations using parallel platens (misalignment of 0°) or using platens misaligned similarly to the experimental set-up (misalignment of 0.25° in both x- and y-direction) resulted in almost identical results (not shown here). Therefor, platen

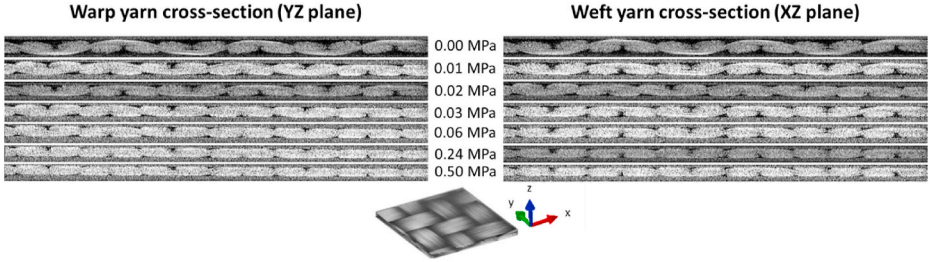

Fig. 6. µCT images of the yarn cross-sections during compression.

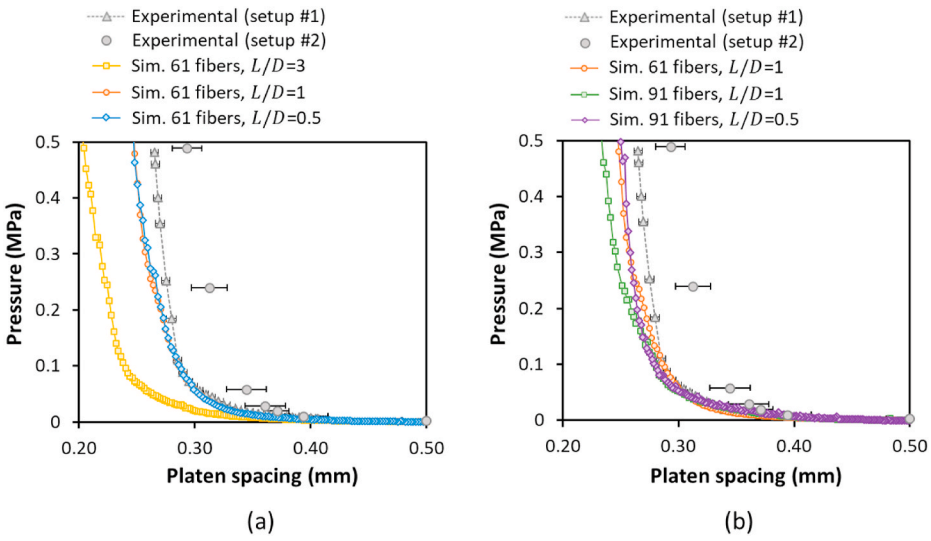

Fig. 7. Compressive response for (a) different L/D ratios and (b) different amounts of virtual fibers per yarn n_{vf} show that the compressive response converges for $L/D \leq 1$ and $n_{vf} \geq 61$.

misalignment is not further considered in the simulations.

4.3.2. Bending stiffness

The need to add virtual fiber bending stiffness to the simulation is illustrated in Fig. 8 by the difference in the compression reaction force of the fabric when bending stiffness is and is not present. Simulations performed without any bending stiffness mainly show a kinematic response where initially the reaction force is predominantly determined by the ease with which the (virtual) fibers can be rearranged in the structure by the compression platens (densification). The reaction force on the platens only increases at high compression levels when fiber realignment becomes obstructed and the fibers become transversally loaded. On the other hand, when including fiber bending stiffness, the kinematics remain fairly similar, but an additional compressive reaction force is noted, especially in the low pressure range. At this stage, the platens deform the virtual fibers by bending – as well as realigning – them. The compressive response shows better agreement with the experimentally determined curve, both in terms of its shape and its position.

The question arises which value for the bending stiffness should be included in the simulations. Experimentally, the bending stiffness of yarns is usually determined through Peirce's cantilever method (Fig. 9a, method 1). Herein, the length of yarn required to have a deflection of 41.5° under the yarn's weight is recorded, which is then converted to a bending stiffness in *Nm*. Although historically important and still widely used, the method is limited since the bending stiffness is assumed to be constant and measured at relatively high curvature. As yarns are a fibrous material, their cross-section easily changes by realignment of the fibers. It is well-known that the yarns can flatten out at high curvatures [36] which likely affects the results.

Theoretically, one can make an estimated guess of the yarn bending stiffness by using beam theory to determine the bending stiffness of a single fiber within that yarn and multiplying that value with the number of fibers present in the yarn (Fig. 9a, method 2). This corresponds to the assumption that the yarn is made up of fibers all lying next to each other on the yarn's heart line without any interaction between them. Hence such a value underestimates the actual yarn bending stiffness. If the position of each of the fibers within the yarn envelope is known, a more realistic approximation of the yarn bending stiffness could be made using the parallel axis theorem. The distance between the fiber bending axis and the yarn bending axis then causes an additional increase in the calculated yarn bending stiffness (Fig. 9a, method 3). An idealized approximation of the fiber positions can be made a priori by assuming that they all lie evenly spaced in layers with a height equal to the fiber

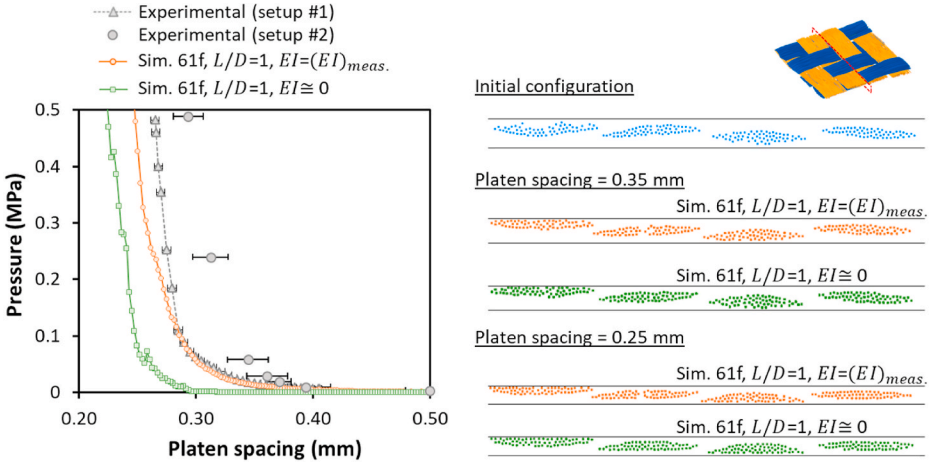

Fig. 8. Compressive response of fabric simulated with and without bending stiffness of the virtual fibers show that while kinematically similar (yarn cross-sections are visualized on the right-hand side), the mechanical response (left-hand side) is better predicted when bending stiffness is considered.

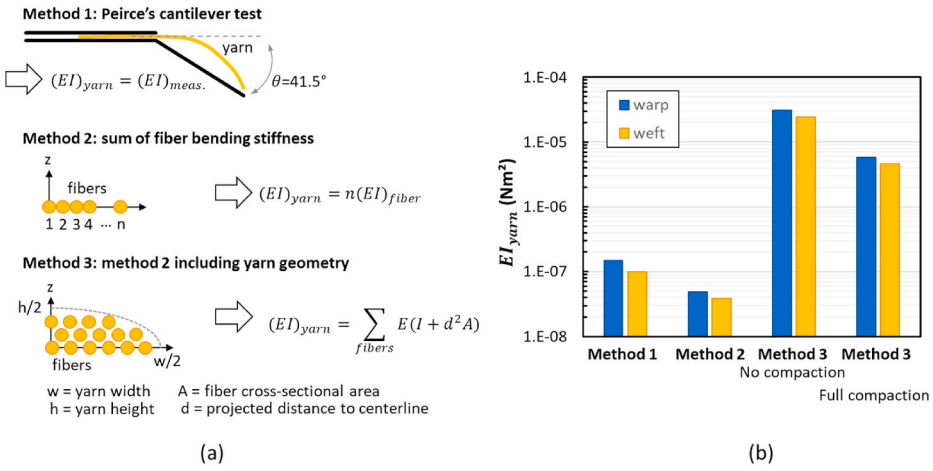

Fig. 9. (a) Calculation of the yarn bending stiffness $(EI)_{yarn}$ through three different methods, and (b) the resulting values of $(EI)_{yarn}$. These results show that the experimentally determined $(EI)_{yarn}$ is at the lower bound of the theoretically calculated range. This indicates that the bending stiffness of the yarns is predominantly determined by the bending stiffness of the individual fibers and much less by their position within the yarn's cross-section, which in turn indicates that fiber realignment is a major deformation mechanism during yarn bending.

diameter in an ellipsoidal configuration that represents the cross-section of the yarn. This assumption would only require the yarn width and height and the number of fibers per yarn and should give a ballpark number for the yarn bending stiffness (not considering fiber-to-fiber interaction).

Fig. 9b shows the values for the bending stiffness that are determined according to the methods described in the previous two paragraphs (experimentally, theoretically without the parallel axis theorem, and theoretically with the parallel axis theorem at two compression levels). It is worth noting that the experimentally determined bending stiffness $(EI)_{measured}$ falls within the range determined by the idealized theoretical calculations which span about three orders of magnitude. Furthermore, $(EI)_{measured}$ is closer to the predicted bending stiffness without applying the parallel axis theorem for the initial yarn shape (height and width measured from μCT images). This is further indication – at least at a curvature responsible for the yarn making a 41.5° angle in Peirce's cantilever experiment – that the measured bending stiffness is strongly influenced by "flattening" of the yarn. This shows that fiber realignment, and the accompanying cross-section change, is a dominant deformation mechanism during the bending of yarns.

Note that Equation (2), used to determine the value of the bending stiffness imposed on each individual virtual fiber, does not take into account the position of the virtual fibres within the yarn and thus does not use the parallel axis theorem. However, as the number of virtual fibers is rather small, the difference in *EI* determined according to 'method 2' and 'method 3' is only around one order of magnitude for the virtual yarns, compared to three orders of magnitude for the real yarns.

Despite these complications, Equation (2) is applied and $(EI)_{yarn} = (EI)_{measured}$ is used as a baseline in the simulations to induce a bending stiffness in the virtual fibers, as bending stiffness measurements according to Peirce's method are readily available in literature. Fig. 10 shows the effect of increasing the bending stiffness by two orders of magnitude on the compressive response of the simulated fabric. Firstly, one can see that the simulations correlate well with the experimentally determined compressive behavior, especially when taking into account the uncertainty on the experimental bending stiffness measurements. For the baseline bending stiffness, the thickness of the fabric at a certain pressure is slightly underestimated. The overall shape of the simulated compressive curve is however close to the experimental compressive, which indicates that the simulation does take the correct deformation mechanisms (e.g. yarn flattening, fiber realignment, …) into account. The agreement between simulation and experiment improves (slightly) for a bending stiffness 2 or 5 times the base bending stiffness. At even higher bending stiffness of 10 and 100 times $(EI)_{measured}$, the compressive response at low compression levels is overestimated, indicating that values in this range are too high. Hence, these simulations show that using Peirce's cantilever method results in an adequate value for the yarn bending stiffness, perhaps slightly underestimating it. Nevertheless, it might be worthwhile to consider other test methods in the future that allow recording of the moment-curvature relationship to obtain better input parameters, e.g. by using apparatus similar to the Kawabata Evaluation System for Fabrics or the set-up described in Ref. [37]. Another possibility would be to explicitly model Peirce's cantilever experiment using virtual fibers to inversely determine the correct

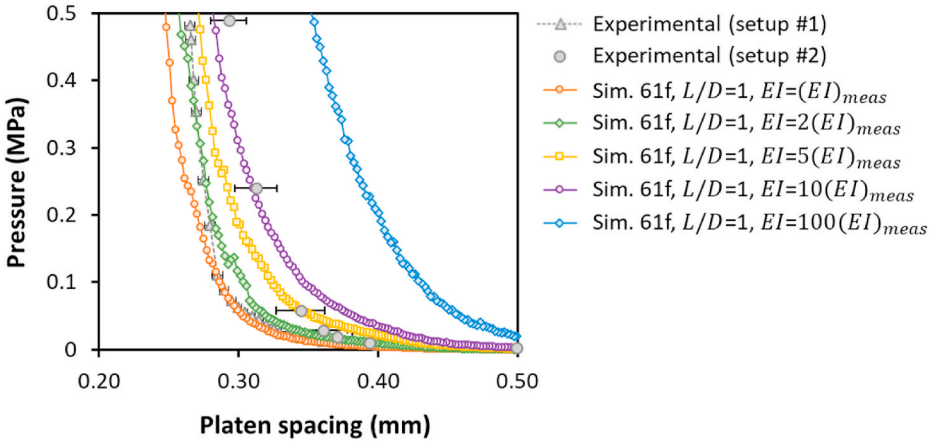

Fig. 10. Effect of the bending stiffness of the virtual fibers on the compressive response of the simulated fabric. A better agreement between the simulated and experimental responses is obtained for a bending stiffness in the range of 2–5 times the $(EI)_{measured}$ (from Peirce's cantilever method).

$(EI)_{yarn}$, but the large displacements required under quasi-static conditions make this approach unfeasible with the current set-up.

4.3.3. Friction coefficient

Contrary to the as-woven simulation, there are (almost) no in-plane tensile forces active during the through-thickness compression, and the deformation happens under quasi-static conditions. Therefore, it is likely that the higher-bound friction coefficient of 0.3–0.4 is more appropriate. Note that there is only one frictional constant allowed in the *General Contact* algorithm of the Abaqus 2019 solver, which determines the interaction between all surfaces, i.e. fiber-to-fiber as well as fiber-to-platen.

Moreover, similar to the bending stiffness, the friction coefficient input value likely depends on the discretization in digital fibers. Since the friction coefficient is typically determined from yarn-to-yarn friction experiments, the amount of contacting surface area is determined by the surface area of the fibers at the yarns' outside perimeter. In addition, as the fibers can realign themselves, intrayarn fiber-to-fiber friction also occurs, while fibers that were present at the "inside" of the yarn might migrate towards the yarn boundary depending on the deformation (e.g. at high compression level). Hence, the yarn's complete surface area $A_{\mu,\,yarn}$, determined by the cylindrical surface of each fiber, comes into play during through-thickness compression. It is clear that this value is highly dependent on the number of fibers as well as their diameter, according to the following equation (per unit length):

$$A_{\mu,yarn} = n_{fiber} A_{\mu,fiber} = \pi\, n_{fiber} D_{fiber} \tag{3}$$

The ratio of the contact surface for the real yarn $A_{\mu,ry}$ to that of the virtual yarn $A_{\mu,vy}$ is determined as:

$$\frac{A_{\mu,ry}}{A_{\mu,vy}} = \frac{n_{rf} D_{rf}}{n_{vf} D_{vf}} = \frac{n_{rf}}{n_{vf}} \left(\frac{n_{rf}}{n_{vf}}\right)^{-\frac{1}{2}} = \left(\frac{n_{rf}}{n_{vf}}\right)^{\frac{1}{2}} \tag{4}$$

and is found to be dependent only on the ratio of real to virtual fibers per yarn. For the number of virtual fibers used here, i.e. 61 and 91, we thus estimate that the internal surface area inside the real yarn is about 5 times higher than that inside the virtual yarn. This shows that using the experimentally determined frictional coefficient as an input value in the simulation likely results in an underestimation of the contact forces. However, one cannot simply multiply this coefficient with a factor of 5, as the kinematics of the actual fibers will also be different from those of the virtual fibers. For example, while the great amount of small fibers in the real yarn results in a lot of potential contact surface, they will also have more freedom to realign themselves and fill in empty gaps between other fibers resulting in overall lower contact forces.

Fig. 11 shows the compressive response for simulations with $EI_{yarn} = EI_{measured}$ for a range of frictional constants from 0.2 to 0.4 which are still physically relevant and correspond to the measured frictional constants, up to values of 0.8 which correspond to artificially increased frictional constants. This shows that higher frictional constants indeed lead to a better correlation between the simulation and the experiment as could be expected. Nevertheless, in general, even a value of 0.35, which corresponds to the measured value at low yarn pressure and low sliding speed, still produces acceptable results (falls within the experimently detetermined range) and is thus a good input parameter.

4.3.4. Hysteresis – losses upon compression-unloading

The implementation of both bending stiffness, as well as friction into the virtual fiber simulations, means that they can be predictive for (frictional) losses upon both compressive loading and unloading. This is illustrated in Fig. 12a and Table 2 by a range of simulations with different parameters (the losses are determined by the area between the loading-unloading curve). The experimental losses were determined from the loading-unloading curves obtained through the compliance-calibration procedure (setup #1). In both simulation and experiment, the fabric is loaded monotonically to 0.5 MPa and immediately unloaded at the same speed while the load-displacement curve is recorded. The results in Table 2 show that the hybrid virtual fibers are indeed capable of simulating hysteresis losses during compression-unloading of a single fabric and the agreement between the experimental and simulated values is good. Moreover, the hysteresis losses seem relatively independent from input parameters such as the bending stiffness and the frictional constant. Fig. 12b shows the (cumulative) frictional dissipated energy (obtained from the history output data in Abaqus) in function of the simulation progress (time). In each of the hysteresis simulations, the trend in frictional dissipated energy was similar, with the strongest increase in dissipated energy happening at the end of the loading step (compaction). Furthermore, after the sharp drop in pressure during unloading, the frictional dissipated energy keeps increasing, albeit at a lower rate. This indicates fiber movement which corresponds to a recovery of the (bending) stresses and spring back of the fibers.

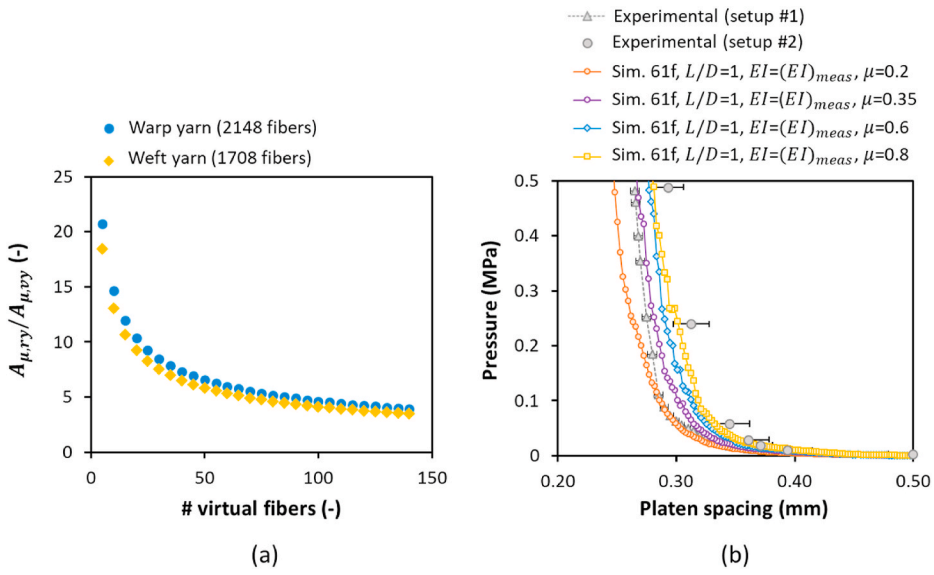

Fig. 11. (a) Ratio of contact surface for the real yarn $A_{\mu,ry}$ to that of the virtual yarn $A_{\mu,vy}$ shows that at 61–91 virtual fibers per yarn, the virtual contact surface is about one fifth the size of the real contact surface. (b) The effect of the frictional constant on the compressive response shows that higher frictional constants result in better agreement with the experimentally determined response.

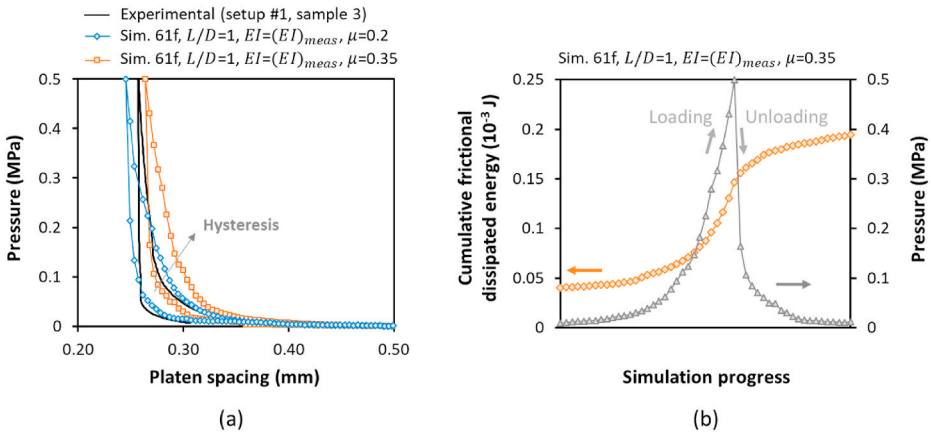

Fig. 12. (a) Experimental and simulated (61 fibers, $L/D = 1$, $EI = (EI)_{meas}$, $\mu = 0.2$, and 61 fibers, $L/D = 1$, $EI = (EI)_{meas}$, $\mu = 0.35$) loading-unloading compressive response of a single fabric layer. Overall, the curve shape is well predicted by the simulations with an immediate and large drop in pressure at the start of unloading. (b) The frictional dissipated energy obtained from the history output data of Abaqus in function of simulation progress shows that the main frictional dissipation occurred at high compaction pressures during the loading step. After the immediate pressure drop during unloading, the frictional dissipated energy still increases slightly, indicating some fiber movement during unloading (spring back).

Table 2
Hysteresis losses during loading-unloading of the fabric layer. The experimental value is determined from the curves obtained by the compliance-calibration procedure (setup #1). The simulated values are higher, but correspond well to the experimental value.

Experiment					Hysteresis losses (J/m^2)
					6.72 ± 0.24
Simulation	**# virtual fibers**	***L/D***	***EI***	***μ***	
	61	1	EI_{meas}	0.2	7.62
	61	1	EI_{meas}	0.35	8.04
	61	1	EI_{meas}	0.6	7.15
	61	1	EI_{meas}	0.8	7.06
	61	1	$2EI_{meas}$	0.35	7.92

4.3.5. *Contact problems arising at high pressure levels*

The General Contact algorithm implemented in Abaqus/Explicit is very robust at detecting colliding/contacting surfaces for truss elements. Yet it is a kinematically enforced algorithm, meaning that in each time step, the surfaces are allowed to move "into" each other at a ratio of k (penalty stiffness), resulting in an opposing contact force which is then iterated and resolved to have proper surface-to-surface contact. The downside to such an algorithm – in this case – is that numerical softening (and damping) is required. The softening prevents extreme static loadings. This might be a reason why the simulated compressive response is always slightly lacking in stiffness at high compression (lower slope compared to the experimental data, see e.g. Fig. 10). More importantly, with the current implementation using the standard numerical settings, where the penalty stiffness is automatically determined by the software based on the material properties, the amount of compressive pressure is limited to approximately 1 MPa. At pressures above this value, the penetration of contacting surfaces becomes very prominent and affects the predictive capability of the simulation method as the fabric thickness is underestimated, see Fig. 13. Nevertheless, pressures relevant for vacuum infusion and autoclave production from 0 to 8 bar remain viable.

5. Conclusions

The results clearly show the potential for the virtual fiber modeling method including fiber bending stiffness as a general textile modeling framework. Taking our previous work on in-plane properties into account [18,19], the addition of out-of-plane property simulation

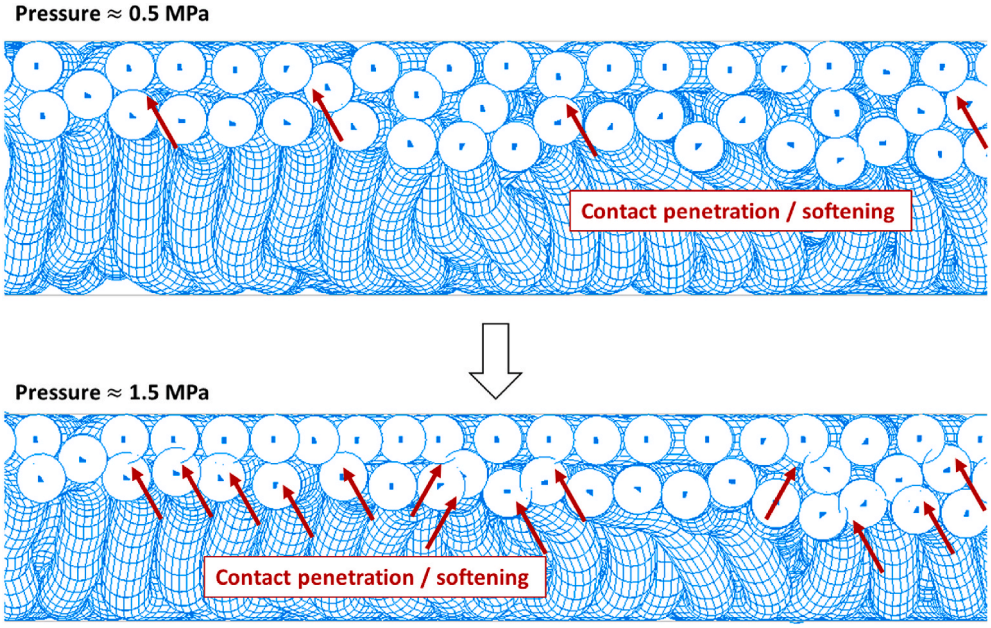

Fig. 13. Contact overclosures/penetrations (softening) between neighboring fibers occur in large amounts at pressures above 1 MPa.

capabilities indicates that a large range of textile-relevant loadings can be considered. This approach, fully implemented in the commercial finite element software package Abaqus using the standard element, material and contact libraries, allows research groups with FEA experience but without dedicated virtual fiber tools to implement this type of modeling. Good agreement is obtained between the experimental and the numerical determined pressure-compression behavior. The macroscopic compressive response of the fabric is well predicted for the right set of input parameters. Moreover, the microscale deformation mechanisms are captured as well, resulting in good agreement with μCT-scans and prediction of hysteresis-losses due to fiber realignment and friction.

On the other hand, the results also show that improvements are still required. For example, an L/D element ratio of 1 was used in this work, but larger ratios could improve computation time. Yet, here, L/D ratios of 3 result in non-converged solutions. One possible solution could be the use of non-constant element lengths along the fiber to reduce the number of elements while maintaining convergence. On the input property side, the friction coefficient and bending stiffness that should be implemented remain difficult to assess. Although the results have shown that the simulation output is rather robust for a wide range of input properties, it would be best to determine which values are most appropriate. Future studies could, for example, consider a numerical calibration of the material parameters by using a 1-to-1 simulation-experimental approach, where the -previously experimental - friction and bending stiffness experiments are explicitly modeled using virtual fibers. In addition, more complex material behavior such as non-linear bending and non-linear friction can be included to increase the prediction accuracy. To extend the method to high-pressure LCM processes, a robust contact algorithm with minimal contact penetration is required.

Overall, the proposed methods allow a predictive analysis of fabric compression behavior and are thus well-suited to analyze and optimize fabric structures for example in LCM manufacturing processes.

CRediT authorship contribution statement

Lode Daelemans: Conceptualization, Methodology, Investigation, Funding acquisition, Writing - original draft, Writing - review & editing. **Brecht Tomme:** Conceptualization, Methodology, Investigation, Writing - review & editing. **Baris Caglar:** Conceptualization, Investigation, Writing - review & editing. **Véronique Michaud:** Supervision, Resources, Funding acquisition, Writing - review & editing. **Jeroen Van Stappen:** Investigation, Writing - review & editing. **Veerle Cnudde:** Resources, Writing - review & editing. **Matthieu Boone:** Validation, Resources, Writing - review & editing. **Wim Van Paepegem:** Conceptualization, Methodology, Supervision, Resources, Funding acquisition, Writing - original draft, Writing - review & editing.

Declaration of competing interest

The authors declare that they have no known competing financial interests or personal relationships that could have appeared to influence the work reported in this paper.

Acknowledgments

Financial support from Research Foundation – Flanders (FWO, Belgium) is gratefully acknowledged. Results in this paper were obtained within the framework of the FWO grant 12 ZR520N. For the CT5000 load cell, FCWO – UGent (Belgium), as well as FWO is acknowledged under the project G.0041.15N. The Centre of Expertise UGCT is supported by the Ghent University Special Research Fund (BOF. EXP.2017.0007, Belgium). We acknowledge the Swiss Competence Center for Energy Research (SCCER, Switzerland), Mobility of the Swiss Innovation Agency (Innosuisse, Switzerland) and the Swiss National Science Foundation (SNF - 182669, Switzerland) for financial support.

References

[1] J. Hemmer, C. Burtin, S. Comas-Cardona, C. Binetruy, T. Savart, A. Babeau, Unloading during the infusion process: direct measurement of the dual-scale fibrous microstructure evolution with X-ray computed tomography, Compos. Part A Appl. Sci. Manuf. 115 (2018) 147–156, https://doi.org/10.1016/j.compositesa.2018.09.013.

[2] W. Huang, P. Causse, H. Hu, S. Belouettar, F. Trochu, Transverse compaction of 2D glass woven fabrics based on material twins – Part I: geometric analysis, Compos. Struct. 237 (2020) 111929, https://doi.org/10.1016/j.compstruct.2020.111929.

[3] M.A. Ali, R. Umer, K.A. Khan, W.J. Cantwell, In-plane virtual permeability characterization of 3D woven fabrics using a hybrid experimental and numerical approach, Compos. Sci. Technol. 173 (2019) 99–109, https://doi.org/10.1016/j.compscitech.2019.01.030.

[4] Y. Mahadik, K.A.R. Brown, S.R. Hallett, Characterisation of 3D woven composite internal architecture and effect of compaction, Compos. Part A Appl. Sci. Manuf. 41 (2010) 872–880, https://doi.org/10.1016/j.compositesa.2010.02.019.

[5] T. Centea, P. Hubert, Measuring the impregnation of an out-of-autoclave prepreg by micro-CT, Compos. Sci. Technol. 71 (2011) 593–599, https://doi.org/10.1016/j.compscitech.2010.12.009.

[6] S.C. Garcea, Y. Wang, P.J. Withers, X-ray computed tomography of polymer composites, Compos. Sci. Technol. 156 (2018) 305–319, https://doi.org/10.1016/j.compscitech.2017.10.023.

[7] S. Yan, X. Zeng, L. Brown, A. Long, Geometric modeling of 3D woven preforms in composite T-joints, Textil. Res. J. 88 (2018) 1862–1875, https://doi.org/10.1177/0040517517712098.

[8] Z. Yousaf, P. Potluri, F. Léonard, P. Withers, Meso scale analysis of 2D glass woven preforms under compaction, in: ICCM Int. Conf. Compos. Mater., International Committee on Composite Materials, 2013, pp. 392–399.

[9] M. Valkova, D.B. Anthony, A.R.J. Kucernak, M.S.P. Shaffer, E.S. Greenhalgh, Predicting the compaction of hybrid multilayer woven composite reinforcement stacks, Compos. Part A Appl. Sci. Manuf. 133 (2020) 105851, https://doi.org/10.1016/j.compositesa.2020.105851.

[10] Y. Wang, X. Sun, Digital-element simulation of textile processes, Compos. Sci. Technol. 61 (2001) 311–319, https://doi.org/10.1016/S0266-3538(00)00223-2.

[11] G. Zhou, X. Sun, Y. Wang, Multi-chain digital element analysis in textile mechanics, Compos. Sci. Technol. 64 (2004) 239–244, https://doi.org/10.1016/S0266-3538(03)00258-6.

[12] O. Döbrich, T. Gereke, C. Cherif, Modeling the mechanical properties of textile-reinforced composites with a near micro-scale approach, Compos. Struct. 135 (2016) 1–7, https://doi.org/10.1016/j.compstruct.2015.09.010.

[13] D. Durville, I. Baydoun, H. Moustacas, G. Périé, Y. Wielhorski, Determining the initial configuration and characterizing the mechanical properties of 3D angle-interlock fabrics using finite element simulation, Int. J. Solid Struct. (2017), https://doi.org/10.1016/j.ijsolstr.2017.06.026.

[14] D. Durville, Simulation of the mechanical behaviour of woven fabrics at the scale of fibers, Int. J. Material Form. 3 (2010) 1241–1251, https://doi.org/10.1007/s12289-009-0674-7.

[15] S.D. Green, A.C. Long, B.S.F. El Said, S.R. Hallett, Numerical modelling of 3D woven preform deformations, Compos. Struct. 108 (2014) 747–756, https://doi.org/10.1016/j.compstruct.2013.10.015.

[16] Y. Mahadik, S.R. Hallett, Finite element modelling of tow geometry in 3D woven fabrics, Compos. Part A Appl. Sci. Manuf. 41 (2010) 1192–1200, https://doi.org/10.1016/j.compositesa.2010.05.001.

[17] L. Huang, Y. Wang, Y. Miao, D. Swenson, Y. Ma, C.-F. Yen, Dynamic relaxation approach with periodic boundary conditions in determining the 3-D woven textile micro-geometry, Compos. Struct. 106 (2013) 417–425, https://doi.org/10.1016/j.compstruct.2013.05.057.

[18] L. Daelemans, J. Faes, S. Allaoui, G. Hivet, M. Dierick, L. Van Hoorebeke, W. Van Paepegem, Finite element simulation of the woven geometry and mechanical behaviour of a 3D woven dry fabric under tensile and shear loading using the digital element method, Compos. Sci. Technol. 137 (2016) 177–187, https://doi.org/10.1016/j.compscitech.2016.11.003.

[19] T.D.D. Dinh, A. Rezaei, L. Daelemans, M. Mollaert, D. Van Hemelrijck, W. Van Paepegem, A hybrid micro-meso-scale unit cell model for homogenization of the nonlinear orthotropic material behavior of coated fabrics used in tensioned membrane structures, Compos. Struct. 162 (2017) 271–279, https://doi.org/10.1016/j.compstruct.2016.12.027.

[20] Z. Yousaf, P. Potluri, P.J. Withers, D. Mollenhauer, E. Zhou, S. Duning, Digital element simulation of aligned tows during compaction validated by computed tomography (CT), Int. J. Solid Struct. 154 (2018) 78–87, https://doi.org/10.1016/j.ijsolstr.2017.05.044.

[21] A.J. Thompson, B. El Said, D. Ivanov, J.P.H.P.-H. Belnoue, S.R. Hallett, High Fidelity Modelling of the Compression Behaviour of 2D Woven Fabrics, Elsevier Ltd, n.d. doi:10.1016/j.ijsolstr.2017.06.027.

[22] Q.T. Nguyen, E. Vidal-Sallé, P. Boisse, C.H. Park, A. Saouab, J. Bréard, G. Hivet, Mesoscopic scale analyses of textile composite reinforcement compaction, Compos. B Eng. 44 (2013) 231–241, https://doi.org/10.1016/j.compositesb.2012.05.028.

[23] A. Charmetant, E. Vidal-Sallé, P. Boisse, Hyperelastic modelling for mesoscopic analyses of composite reinforcements, Compos. Sci. Technol. 71 (2011) 1623–1631, https://doi.org/10.1016/j.compscitech.2011.07.004.

[24] W. Wijaya, S. Bickerton, P.A. Kelly, Meso-scale compaction simulation of multi-layer 2D textile reinforcements: a Kirchhoff-based large-strain non-linear elastic constitutive tow model, Compos. Part A Appl. Sci. Manuf. 137 (2020) 106017, https://doi.org/10.1016/j.compositesa.2020.106017.

[25] A.J. Thompson, J.R. McFarlane, J.P.H. Belnoue, S.R. Hallett, Numerical modelling of compaction induced defects in thick 2D textile composites, Mater. Des. 196 (2020) 109088, https://doi.org/10.1016/j.matdes.2020.109088.
[26] L. Montero, S. Allaoui, G. Hivet, Characterisation of the mesoscopic and macroscopic friction behaviours of glass plain weave reinforcement, Compos. Part A Appl. Sci. Manuf. 95 (2017) 257–266, https://doi.org/10.1016/j.compositesa.2017.01.022.
[27] D. Salvatori, B. Caglar, V. Michaud, 3D spacers enhance flow kinetics in resin transfer molding with woven fabrics, Compos. Part A Appl. Sci. Manuf. 119 (2019) 206–216, https://doi.org/10.1016/j.compositesa.2019.01.023.
[28] S.V. Lomov, L. Gorbatikh, Ž. Kotanjac, V. Koissin, M. Houlle, O. Rochez, M. Karahan, L. Mezzo, I. Verpoest, Compressibility of carbon woven fabrics with carbon nanotubes/nanofibres grown on the fibres, Compos. Sci. Technol. 71 (2011) 315–325, https://doi.org/10.1016/j.compscitech.2010.11.024.
[29] M. Dierick, D. Van Loo, B. Masschaele, J. Van Den Bulcke, J. Van Acker, V. Cnudde, L. Van Hoorebeke, Recent micro-CT scanner developments at UGCT, Nucl. Instrum. Methods Phys. Res. Sect. B Beam Interact. Mater. Atoms 324 (2014) 35–40, https://doi.org/10.1016/j.nimb.2013.10.051.
[30] J. Vlassenbroeck, M. Dierick, B. Masschaele, V. Cnudde, L. Van Hoorebeke, P. Jacobs, Software tools for quantification of X-ray microtomography at the UGCT, Nucl. Instruments Methods Phys. Res. Sect. A Accel. Spectrometers, Detect. Assoc. Equip. 580 (2007) 442–445, https://doi.org/10.1016/j.nima.2007.05.073.
[31] S. Comas-Cardona, P. Le Grognec, C. Binetruy, P. Krawczak, Unidirectional compression of fibre reinforcements. Part 1: a non-linear elastic-plastic behaviour, Compos. Sci. Technol. 67 (2007) 507–514, https://doi.org/10.1016/j.compscitech.2006.08.017.
[32] Q. Govignon, S. Bickerton, P.A. Kelly, Simulation of the reinforcement compaction and resin flow during the complete resin infusion process, Compos. Part A Appl. Sci. Manuf. 41 (2010) 45–57, https://doi.org/10.1016/j.compositesa.2009.07.007.
[33] B. Yenilmez, E.M. Sozer, Compaction of e-glass fabric preforms in the vacuum infusion process, A: characterization experiments, Compos. Part A Appl. Sci. Manuf. 40 (2009) 499–510, https://doi.org/10.1016/j.compositesa.2009.01.016.
[34] Y. Wang, Y. Miao, D. Swenson, B.A. Cheeseman, C.-F. Yen, B. LaMattina, Digital element approach for simulating impact and penetration of textiles, Int. J. Impact Eng. 37 (2010) 552–560, https://doi.org/10.1016/j.ijimpeng.2009.10.009.
[35] Y. Miao, E. Zhou, Y. Wang, B.A. Cheeseman, Mechanics of textile composites: micro-geometry, Compos. Sci. Technol. 68 (2008) 1671–1678, https://doi.org/10.1016/j.compscitech.2008.02.018.
[36] B. Cornelissen, R. Akkerman, Analysis of yarn bending behaviour, in: 17th Int. Conf. Compos. Mater. (ICCM 17), The British Composites Society, 2009.
[37] H. Alshahrani, M. Hojjati, A new test method for the characterization of the bending behavior of textile prepregs, Compos. Part A Appl. Sci. Manuf. 97 (2017) 128–140, https://doi.org/10.1016/j.compositesa.2017.02.027.